

the  $x$  and  $y$  directions of the network of dots, solitons can be propagated along chains that turn corners. There is, in principle, no physical problem in splitting a soliton into two channels, and so fan-out of signals should also be possible. Further simulations show that NOT functions, concatenated gates, and crossing chains are also possible [see (9) for electronic QCA implementations]. The fact that they operate at room temperature and are fabricated from a size of dot that could be manufactured commercially makes them ideal candidates for integration into microelectronic hardware. Input dots could be programmed locally by passing an electrical current through a conducting track underneath the dot, as in magnetic random access memory (10, 11). Signal output could be obtained from single dots in a complex network by using one of the recently discovered magnetoelectronic effects (10).

Power gain is a very important issue in all QCA architectures. Electronic QCA circumvents this by temporarily removing the energy barriers between logic states during switching, to allow near-adiabatic operation (12). In principle, MQCA solitons propagate without loss and so should be able to mediate a logic switch without any dissipation; in practice, small fluctuations in the shape of the dots will lead to anisotropy fluctuations (the size of dots reported here gain  $\sim 10$  Oe of anisotropy field for each percent of ellipticity in shape), which will cause the soliton to dissipate energy as it propagates. In our MQCA architecture, this energy is provided by the externally applied oscillating magnetic field. Power gain to overcome losses and to enable fan-out of signals can thus be achieved.

The need to minimize anisotropy fluctuations places a required accuracy on the circularity of the dots of better than  $\pm 2\%$ . We can infer from the signal level of Fig. 2C that this accuracy has been achieved in at least 19 of the 20 networks that we fabricated using only conventional electron beam lithography. Furthermore, this fabrication requirement is one order of magnitude less stringent than that of electronic QCA (13).

MQCA has enormous potential to meet the future requirements of microelectronics for digital processing. If we take a single MQCA dot to be analogous to a transistor (comparing different paradigms is difficult, but this allows for an order of magnitude comparison), then the unoptimized device we report here has an integration density of 5500 million  $\text{cm}^{-2}$ , compared with 6.6 million  $\text{cm}^{-2}$  for today's CMOS technology (14). The magnetostatic interaction energy between two of the dots reported here is  $200 k_B T$  ( $k_B$  is Boltzmann's constant and  $T$  is room temperature). An energy of at least  $40 k_B T$  is required if thermally induced data errors are to be kept below one per year. MQCA should therefore be very stable

against thermal fluctuations. Simple scaling laws show that this will remain the case for dots as small as 20 nm in diameter, giving a possible integration density of 250,000 million  $\text{cm}^{-2}$ . The maximum energy that any magnetic object of volume  $V$  can dissipate in one field cycle of peak-to-peak amplitude  $H$  is  $8\pi M_s H V$  ( $M_s$  is the saturation magnetization in centimeter-gram-second units), which gives a maximum dot dissipation of  $10^{-17}$  J per clock cycle (for the size of dots described here). This is  $10^4$  times less than the power-delay product of  $10^{-13}$  J for today's CMOS (15), meaning that a microprocessor based on MQCA would typically dissipate around only 1 W. Recent studies (16) have shown that submicrometer magnetic particles can be switched in less than 1 ns. This gives a conservative estimate on the order of 100 MHz for the maximum expected across-chip clock frequency of MQCA devices, although full dynamic calculations and experiments will be essential to determine the influence of spin-wave excitations. The fact that entire networks can be constructed on a single plane means that many planes could in principle be stacked on top of each other, thus giving a way to realize three-dimensional hardware.

References and Notes

1. R. R. Schaller, *IEEE Spectrum* **34** (no. 6), 52 (1997).
2. M. Schulz, *Nature* **399**, 729 (1999).
3. H. Ahmed and K. Nakazato, *Microelectron. Eng.* **32**, 297 (1996); K. K. Likharev, *Proc. IEEE* **87**, 606 (1999).
4. I. Amlani et al., *Science* **284**, 289 (1999).
5. R. P. Cowburn, D. K. Koltsov, A. O. Adeyeye, M. E. Welland, D. M. Tricker, *Phys. Rev. Lett.* **83**, 1042 (1999).
6. R. P. Cowburn, A. O. Adeyeye, M. E. Welland, *N. J. Phys.* **1**, 16 (1999).
7. R. P. Cowburn, D. K. Koltsov, A. O. Adeyeye, M. E. Welland, *Appl. Phys. Lett.* **73**, 3947 (1998).
8. A. Hubert and R. Schäfer, in *Magnetic Domains: The Analysis of Magnetic Microstructure* (Springer, Berlin, 1998), p. 24.
9. W. Porod et al., *Int. J. Electron.* **86**, 549 (1999).
10. W. J. Gallagher et al., U.S. Patent 5 640 343 (1997).
11. G. A. Prinz, *Science* **283**, 5400 (1999).
12. C. S. Lent and P. D. Tougaw, *Proc. IEEE* **85**, 541 (1997).
13. C. G. Smith, *Science* **284**, 274 (1999).
14. Semiconductor Industry Association International Technology Roadmap for Semiconductors 1999 (Sematech, Austin, TX, 1999); www.sematech.org
15. R. Compañó, L. Molenkamp, D. J. Paul, *Technology Roadmap for European Nanoelectronics* (1999), p. 12.
16. R. L. Stamps and B. Hillebrands *Appl. Phys. Lett.* **75**, 1143 (1999); A. V. Pohm, J. M. Anderson, R. S. Beech, J. M. Daughton, *J. Appl. Phys.* **85**, 4771 (1999); S. E. Russek, J. O. Oti, S. Kaka, E. Y. Chen, *J. Appl. Phys.* **85**, 4773 (1999).
17. R.P.C. was supported by St. John's College, Cambridge.

11 November 1999; accepted 18 January 2000

## Rippling Instability of a Collapsing Bubble

Rava da Silveira,<sup>1</sup> Sahraoui Chaïeb,<sup>2</sup> L. Mahadevan<sup>2</sup>

When a bubble of air rises to the top of a highly viscous liquid, it forms a dome-shaped protuberance on the free surface. Unlike a soap bubble, it bursts so slowly as to collapse under its own weight simultaneously, and folds into a wavy structure. This rippling effect occurs for both elastic and viscous sheets, and a theory for its onset is formulated. The growth of the corrugation is governed by the competition between gravitational and bending (shearing) forces and is exhibited for a range of densities, stiffnesses (viscosities), and sizes—a result that arises less from dynamics than from geometry, suggesting a wide validity. A quantitative expression for the number of ripples is presented, together with experimental results that support the theoretical predictions.

Every day, nature surprises us with structures and patterns of such beauty as to fill the scientist with wonder and the artist with envy. Here, we address an instability that turns a hemispherical, smooth, liquid bubble into a striking wrinkled structure, first observed by Debrégeas, de Gennes, and Brochard-Wyart (1). In their experiment, 0.1 to 10  $\text{cm}^3$  of air injected into a highly viscous liquid (with viscosity  $\eta \sim 10^3$  Pa-s) rises to the free surface, imprisoned in a hemispherical bubble of thickness  $t \sim 1$  to 10  $\mu\text{m}$ . If the bubble is punctured at its apex by a needle,

surface tension drives the rapid expansion of a circular opening. After about 10 to 30 ms, the retraction velocity saturates to a constant, owing to the high viscous resistance. In the meantime, the air flow through the hole equilibrates the pressure difference, allowing the bubble to collapse under its own weight. As it deflates, an instability appears: The fluid sheet folds into a wavy structure, with radial ripples that break the original axisymmetry. In the absence of a detailed theory, a scaling estimate has been proposed (1) for the number of ripples:  $n^* \sim (\mu g R^3 / K)^{1/2}$ , where  $\mu$  is the mass of the film per unit area,  $g$  is the gravitational acceleration,  $R$  is the radius of the hole, and  $K$  is an effective bending rigidity of the sheet (which was assumed to be

<sup>1</sup>Department of Physics, <sup>2</sup>Department of Mechanical Engineering, Massachusetts Institute of Technology, Cambridge, MA 02139, USA.

elastic during the early stages of the rippling).

The rippling results from the competition among compression, bending, and gravity. Each fluid element tends to fall under its own weight but experiences a viscous resistance from its neighborhood. If the bubble were to collapse in a uniform, symmetric way, it would occupy a progressively reduced area, leading to an in-plane compression, which would require forces that far exceed the scale set by gravity. Instead, the film deforms in a nearly inextensional fashion by undergoing pure bending. Equivalently, for a given (gravitational) force, the relative time scale associated with stretching is much larger than that for bending, and the surface therefore corrugates over short times before eventually relaxing into a uniform, thicker membrane.

This instability is reminiscent of buckling phenomena (2), originally studied in the context of elastic rods but also occurring in the creeping flows of viscous liquid filaments [a striking everyday example being the coiling of a stream of honey when it reaches a piece of toast (3, 4)]. For an elastic rod, buckling occurs at the longest possible wavelength in order to minimize the bending energy. In the bubble problem, however, gravity plays a distinctive role in determining the configuration. For a given amplitude, bending still favors large-scale deformations, whereas gravitational energy is minimized for an almost flat sheet with as many tiny ripples as possible; the optimal wavelength results from a compromise between the two. Such an argument, however, does not fully characterize the effect. Unlike the above examples, here the system under consideration is a curved two-dimensional sheet, and the associated geometry constrains the rippling both qualitatively and quantitatively (see below).

The instability occurs in both elastic (solid) and viscous (liquid) films. The elastic case corresponds to a shell with a hole of radius  $R$ , allowed to collapse under its own weight. In the viscous case, an additional complication arises

because the radius of the hole changes during the rippling. After a short initial transient, the hole grows steadily at a rate  $v \sim \sigma/\eta$  resulting from the balance of surface tension ( $\sigma \approx 20$  mN/m) and viscous stress. It thus takes a time  $\tau \sim \eta t/\sigma$  for the opening radius to increase by  $t$ . During this time, the liquid acquires a velocity  $V \sim g\tau$  due to gravity, larger than  $v$  by a factor  $V/v \sim 10^7$ . Even if the liquid is viscoelastic, so that the retraction velocity is enhanced by a factor  $R/t$  ( $\sim 10$  to  $10^4$ ) (1, 5), the hole radius remains essentially constant while the instability occurs (Fig. 1). We may therefore treat the hole radius  $R$  as a given parameter in the theory (6).

Although the bubble has the geometry of a sphere before collapsing, it is quite flattened by the time the ripples appear (Fig. 1B). For simplicity, we consider the unperturbed configuration to be a shallow cone of slope  $\alpha \ll 1$ , described by its height above the surface,

$$h = \alpha(r_0 - r) \quad (1)$$

where  $r$  is the cylindrical radial coordinate and  $r_0$  is the radius of the base. Any deformation of  $h$  introduced by the rippling may be written, without loss of generality, as

$$h + \delta h = \alpha(r_0 - r) - \delta\alpha(r) + \sum_{n \geq 1} [\delta\beta_n^{(1)}(r) \cos(n\theta) + \delta\beta_n^{(2)}(r) \sin(n\theta)] \quad (2)$$

where  $\theta$  is the azimuthal angle. The perturbation  $\delta\alpha$  represents a uniform ( $n$  independent) flattening accompanying the growth of ripples of amplitude  $\delta\beta_n^{(i)}$ , and a crucial step consists in understanding their form and interdependence.

In the case of a thin elastic (viscous) sheet, the two primary modes of deformation are in-plane stretching (shearing) and out-of-plane bending. A generic deformation of an elastic cone (made of a material with Young modulus  $Y$ ), of amplitude  $\zeta$  on a scale  $\ell$ , requires stretch-

ing forces (per unit surface) of order  $Y\zeta/\ell^2$  but much smaller stretching forces (per unit surface) of order  $Y^2\zeta/\ell^4$  (7), so that for a given external drive (gravity in our case), inextensional deformations are greatly preferred (8). In the case of a highly viscous sheet, forces arise from velocity gradients, thus introducing a dynamical element into the problem. However, their dependence on  $t$  and  $\ell$  (essentially due to the variation of the strain across the film) is similar, so that inextensional deformations are again largely favored if  $t \ll \ell \approx r_0/n^*$ . (This condition is satisfied if the selected number of ripples  $n^*$  is small relative to  $10^3$ , as in the present case; see below.) Equivalently, for a given loading, the time scale corresponding to bending is smaller than that for stretching by a factor  $(t/\ell)^2$  (9, 10). Thus, at the onset of the instability, perturbations of the cone must preserve its metric. This requirement translates into the constraints (11)

$$\delta\beta_n^{(i)}(r) = \delta\beta_n^{(i)} \times r + \delta\beta_n^{(i)'} \quad (3)$$

where  $\delta\beta_n^{(i)}$  and  $\delta\beta_n^{(i)'}$  are constants, and

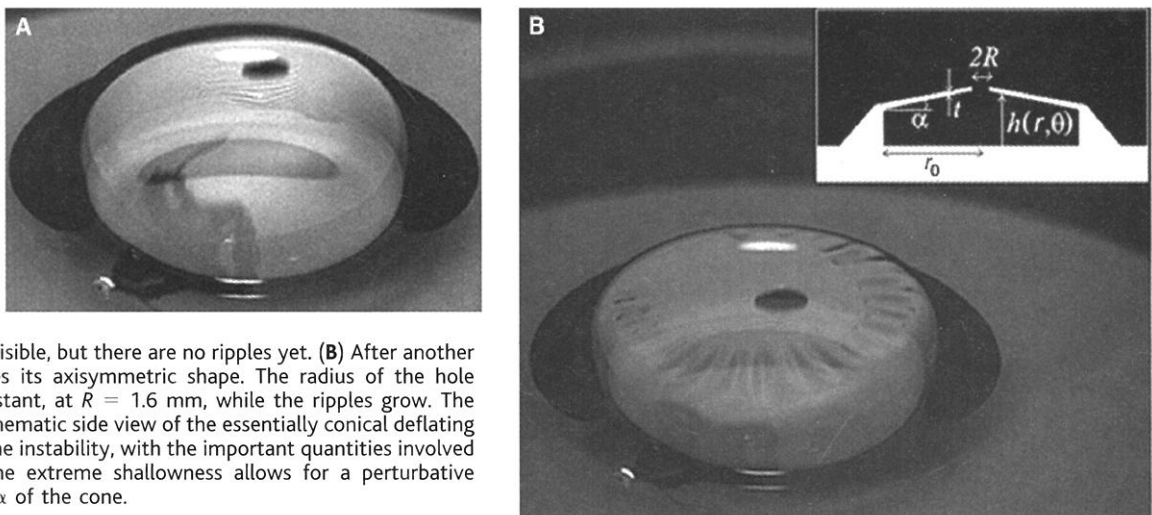
$$4\alpha\delta\alpha(r) = \sum_{n \geq 1, i} [(n^2 - 1)\delta\beta_n^{(i)2}(r - r_0) + n^2\delta\beta_n^{(i)2}(1/r - 1/r_0)] \quad (4)$$

In the following, we elucidate the elastic (solid) case before extending our treatment to the viscous (liquid) case. The energy functional of a perturbed elastic cone is

$$E[h + \delta h] = \int_{\text{cone}} d(\text{surface}) \times (\text{gravitational potential energy} + \text{bending potential energy})$$

$$= \int_R^{r_0} r dr \int_0^{2\pi} d\theta \sqrt{1 + [\nabla(h + \delta h)]^2} \times [\mu g(h + \delta h) + (K/2)(\nabla^2 \delta h)^2] \quad (5)$$

**Fig. 1.** Stroboscopic images of a collapsing liquid bubble of size  $r_0 = 1$  cm and thickness  $t \approx 100$   $\mu\text{m}$ . The silicone oil has viscosity  $\eta = 10^3$  Pa·s, surface tension  $\sigma = 21$  mN/m, and mass density  $0.98$  g/cm<sup>3</sup>. (A) The bubble 30 ms after the film is punctured by a sharp needle. A retracting hole (radius  $R = 1.4$  mm) is visible, but there are no ripples yet. (B) After another 30 ms, the bubble loses its axisymmetric shape. The radius of the hole remains essentially constant, at  $R = 1.6$  mm, while the ripples grow. The inset in (B) displays a schematic side view of the essentially conical deflating bubble at the onset of the instability, with the important quantities involved in the phenomenon. The extreme shallowness allows for a perturbative treatment in the slope  $\alpha$  of the cone.



where  $K = Yt^3/12(1 - \nu^2)$  is the rigidity and  $\nu$  is the Poisson ratio. Only bending elastic energy appears in  $E$ , because we have confined ourselves to the class of inextensible deformations.

If the elastic cone is attached to the plane on which it rests, so that  $\delta h(r = r_0) = 0$ , Eq. 3 yields  $\delta\beta_n^{(i)'} = -\delta\beta_n^{(i)'}r_0$ . On substituting Eqs. 2 through 4 into Eq. 5 we then obtain, to lowest order in the perturbation,

$$\delta E = E[h + \delta h] - E[h] = (\pi/2)K \cdot f(r_0/R) \cdot \sum_{n \geq 1, i} (\delta\beta_n^{(i)})^2 \{g(r_0/R, \gamma R^3) + 2[\varphi(r_0/R) - \gamma R^3 \psi(r_0/R)]n^2 + n^4\} \equiv \sum_{n \geq 1} \delta E_n \quad (6)$$

where  $\varphi(x)$ ,  $\psi(x)$ ,  $f(x)$ , and  $g(x,y)$  are defined

in (12).  $\gamma^{-1/3} = (\alpha K/\mu g)^{1/3}$  is an intrinsic length scale arising from the competition between gravity and bending elasticity.

Each mode contributes an amount  $\delta E_n$  to the change in energy, and rippling occurs if  $\delta E_n < 0$  for some integer. In general,  $\delta E_n < 0$  for a range of different  $n$ 's; the most negative variation corresponds to the maximally growing perturbation and thus sets the wavelength of the instability. The formulation also yields a "threshold condition"  $\varphi(r_0/R) < \gamma R^3 \psi(r_0/R)$  for the occurrence of rippling. This condition involves the three independent quantities  $\gamma$ ,  $r_0$ , and  $R$ , and may be translated into three corresponding statements: (i) Rippling is suppressed if  $\gamma < \gamma_c(r_0, R) = R^{-3} \varphi/\psi$ , i.e., if the cone is too light or too rigid. (ii) Similarly, no rippling occurs if the hole, or

equivalently the cone, is too small,  $r_0 < r_{0c}(\gamma, R)$ . Azimuthal continuity requires the wavelength of the deformation to be at most of order  $r_0$ , resulting in a forbidding bending cost if  $r_0$  becomes small relative to the intrinsic (energetically determined) scale  $\gamma^{-1/3}$ . (iii) The threshold also depends, quite unexpectedly, on the ratio  $r_0/R$ . The dependence of the symmetric ( $n = 0$ ) mode on the radial coordinate  $r$  is different from that of the rippling ( $n \neq 0$ ) modes, so that the high elastic cost can no longer be justified by gravitational gain if the hole is reduced beyond a critical size. Minimizing  $\delta E$  in Eq. 6 yields the selected number of ripples as

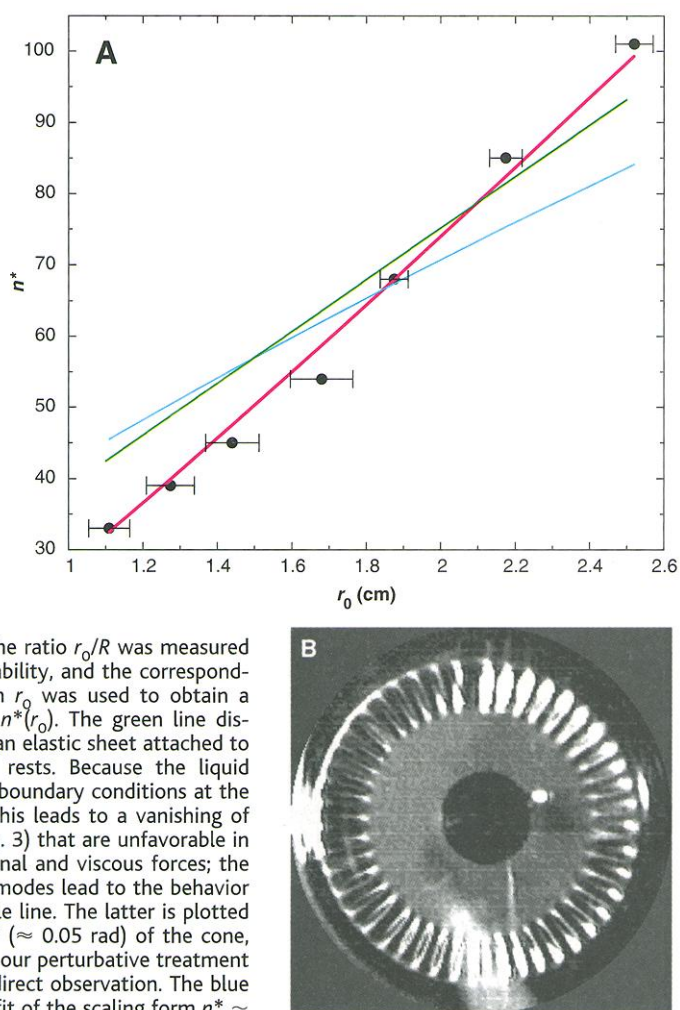
$$n^* = \text{Int} \sqrt{\frac{\mu g R^3}{K} \cdot \frac{1}{\alpha} \psi\left(\frac{r_0}{R}\right) - \varphi\left(\frac{r_0}{R}\right)} \quad (7)$$

where  $\text{Int } x$  is the integer closest to  $x$ . This relation improves on the estimate in (1) (where the authors consider a short-time elastic behavior) and establishes its domain of validity.

For an elastic (solid) sheet, the rippling phenomenon is of an essentially static nature; upon increasing, say, the mass of the sheet, the equilibrium configuration is shifted from symmetric to rippled. Approaching the problem from a dynamical perspective, by considering the elastic forces and torques rather than the corresponding energies, results in an evolution equation  $\pi \mu P(r_0, R) d^2(\delta\beta_n^{(i)})/dt^2 = -\delta E/\delta\beta_n^{(i)}$  for each mode. Here  $P$  is a polynomial function independent of  $n$ , so that the energetically optimal mode, with number  $n^*$ , is indeed the fastest growing one. In the case of a viscous liquid, the effect is intrinsically dynamical: Bending occurs only over short times, whereas the equilibrium configuration is ultimately reached by a slow thickening. Nevertheless, the motion of a viscous film satisfies a formulation close to that of an elastic sheet, as can be shown by integrating the Stokes equation through the thickness (10, 13). Indeed, it is easy to see that bending results from a torque  $\eta t^3/[4(1 - \nu^2)] \times d(\text{curvature})/dt$  analogous to an elastic torque  $K \times (\text{curvature})$ , so that a highly viscous film may be described by an effective bending modulus  $K_t = \eta t^3/3\tau$  ( $\nu = 1/2$  for an incompressible medium), where  $\tau$  is a time scale associated with the falling velocity. Thus, all the conclusions of the stability analysis for the elastic cone, and in particular the expression for the number of ripples (Eq. 7), can be transposed to the case of the bubble except for a certain time scale related to the gravity-induced velocity of the fluid. Comparing the nascent ripples' amplitude with the film thickness yields an estimate of this time scale as  $(t/g)^{1/2}$  (14).

To check our results against experiment, we visualized the bursting of silicone oil bubbles. Once the bubble is punctured with a sharp needle, its evolution is followed using a high-

**Fig. 2. (A)** Plot of the number of ripples  $n^*$  as a function of the bubble radius  $r_0$ , comparing the experimental measures (points) with the theoretical predictions (solid lines). These data were gathered using silicone oil of viscosity  $\eta = 600$  Pa·s and bubbles of thickness  $t \approx 30$   $\mu\text{m}$ . The errors in the measurement of  $r_0$  arise from meniscus effects, which are more important in smaller bubbles. The bursting time elapsed up to rippling is measured to be of order one to five times  $(t/g)^{1/2}$ , consistent with our proposed mechanism for the formation of the corrugation. For each experimental realization, the ratio  $r_0/R$  was measured at the onset of the instability, and the corresponding dependence of  $R$  on  $r_0$  was used to obtain a theoretical curve  $n^* = n^*(r_0)$ . The green line displays the prediction for an elastic sheet attached to the plane on which it rests. Because the liquid cannot be clamped, the boundary conditions at the base must be relaxed. This leads to a vanishing of the unprimed modes (Eq. 3) that are unfavorable in terms of both gravitational and viscous forces; the fastest growing primed modes lead to the behavior represented by the purple line. The latter is plotted here for a slope  $\alpha \approx 3^\circ$  ( $\approx 0.05$  rad) of the cone, which is consistent with our perturbative treatment and in agreement with direct observation. The blue line represents the best fit of the scaling form  $n^* \sim (\mu g R^3/K)^{1/2} (1)$ , where  $R$  is chosen as the relevant length scale. If  $R$  is replaced by  $r_0$ , the above expression for  $n^*$  may be closely fitted (up to an overall multiplicative factor) to our predicted curve, hence the size of the bubble is the dominant length scale within the present experimental range and conditions. This is consistent with the relaxed boundary conditions, which allow the ripples to be appreciable, close to the outer edge of the bubble (see also Fig. 1B). In this way, the ripples trade a bulk gain in gravitational and bending stresses against a cost in stretching in a thin rim close to the outer edge. The increased thickness of the liquid film close to the base further emphasizes this effect, as it reduces the difference in magnitude between a typical stretching and a typical bending stress. **(B)** Top view of the fully developed ripples, from which  $n^*$  is measured.



speed camera capable of recording up to 1000 frames per second. The resulting video is then analyzed to determine the radius  $r_0$  of the bubble, the hole size  $R$  at which the ripples are first observed, and the number of ripples  $n^*$ . Because the hole expands very fast at first,  $R$  is much larger than  $R_c$  by the time the bubble begins to collapse. To compare the experiments with the theory, in which  $R$  enters as a parameter, we measured the latter at the onset of the instability for each given size of the bubble. The quantitative measurements are compared with the theoretical predictions for the dependence of  $n^*$  on the bubble size in Fig. 2. On a more qualitative level, the experiments show a suppression of the instability for small bubbles, in agreement with the threshold conditions above.

We conclude with a discussion of possible refinements of the theory and their relation to the geometric nature of the problem. A more complete theory would incorporate a (flattened) hemisphere as the initial condition, rather than a cone. Also, because of the progressive drainage of the liquid, the thickness  $t$  acquires a dependence on  $r$  (and time). This in turn implies nonuniform rigidity  $K(r)$  and mass  $\mu(r)$ , leading to functions  $f$ ,  $g$ ,  $\varphi$ ,  $\psi$ , and  $P$  of a more complicated form. On a more fundamental level, all these aspects should be addressed in terms of the coupled hydrodynamics of the slow viscous (liquid) flow and the rapid air flow (13). Yet the strong geometrical constraints involved in the problem are suggestive of the robustness of the results.

The question we have answered is akin to that of applying a curved surface onto a flat one in the most economical way, a problem that has taxed cartographers for many centuries and lies at the birth of differential geometry. It is also somewhat of an inverse counterpart to the problem of fitting a flat sheet to a three-dimensional landscape, which has been studied in various contexts (15–17) and is an issue that still vexes fashion designers. The relevance of the geometrical constraints is manifest, for example, in the strong dependence of the rippling on the size of the opening, which is closely related to a well-known theorem by Gauss (18), Jellett (19), and others, according to which (loosely put) a closed surface cannot be bent without being stretched, whereas an open surface can be bent inextensionally. Similarly, we find that a smaller hole implies a relatively stiffer bubble and hampers the rippling. Although the precise forms of the functions  $\varphi$  and  $\psi$  arise from the physical constraints and dynamics imposed by the forces and various boundary conditions, the essence is in the geometry.

References and Notes

1. G. Debrégeas, P.-G. de Gennes, F. Brochard-Wyart, *Science* **279**, 1704 (1998).
2. D. Brush and B. Almroth, *Buckling of Bars, Plates and Shells* (McGraw-Hill, New York, 1975).
3. G. I. Taylor, in *Proceedings of the 12th International Congress of Applied Mechanics* (Springer-Verlag, New York, 1969), p. 382.

4. L. Mahadevan, W. S. Ryu, A. D. T. Samuel, *Nature* **392**, 140 (1998); *Nature* **403**, 502 (2000).
5. G. Debrégeas, P. Martin, F. Brochard-Wyart, *Phys. Rev. Lett.* **75**, 3886 (1995).
6. Whereas surface tension drives the expansion of the hole, rippling is dominated by gravity and viscosity, and we neglect any surface tension-related considerations in the remainder.
7. For a review of elasticity theory, see L. D. Landau and E. M. Lifshitz, *Theory of Elasticity* (Pergamon, New York, ed. 3, 1986); A. E. H. Love, *A Treatise on the Mathematical Theory of Elasticity* (Dover, New York, ed. 4, 1944).
8. The fact that the unperturbed surface is curved plays an essential role here. For a plane, bending energy dominates in the limit of a small deformation, with respect to stretching. For more details, see (7).
9. J. D. Buckmaster, A. Nachman, L. Ting, *J. Fluid Mech.* **69**, 1 (1975).
10. P. D. Howell, *Eur. J. Appl. Math.* **7**, 321 (1996).
11. Exact inextensibility requires that each point on the surface be displaced in the three dimensions in which the cone is imbedded: vertical, radial, and azimuthal. Of course, the three displacements are coupled, but, in the limit  $\alpha \ll 1$ , the radial and angular components are negligibly smaller (by a factor  $\alpha$ ) than the vertical deformation (13). Also, we note that the form of these "inextensibility conditions" depends on the unperturbed configuration, which, in particular, is curved.
12. Here (for  $x \in [1, \infty]$ ),

$$\varphi(x) = \frac{2(x - 1 - \ln x)}{x^2 - 4x + 3 + 2 \ln x} \geq 0$$

$$\psi(x) = \frac{(x - 1)^3}{3(x^2 - 4x + 3 + 2 \ln x)} \geq 0$$

and  $f(x)$ ,  $g(x,y)$  are similar rational functions of  $x$ ,  $\ln x$ , and  $y$ .

13. For the corresponding calculations, see R. da Silveira, S. Chaïeb, L. Mahadevan, in preparation.
14. As the bubble continues to fall, this time scale may vary and so may the number of ripples. However, this last possibility is unlikely, owing to the large forces required to introduce new ripples or remove existing ones.
15. Y. Kantor, M. Kardar, D. R. Nelson, *Phys. Rev. Lett.* **57**, 791 (1986).
16. A. Lobkovsky, S. Gentges, H. Li, D. Morse, T. Witten, *Science* **270**, 1482 (1995).
17. E. Cerda, S. Chaïeb, F. Melo, L. Mahadevan, *Nature* **401**, 46 (1999).
18. M. Spivak, *A Comprehensive Introduction to Differential Geometry* (Publish or Perish, ed. 2, 1979), vol. 1.
19. J. H. Jellett, *Dublin R. Irish Acad. Trans.* **22** (1855).
20. R.d.S. thanks G. Debrégeas for introducing him to the problem and sharing enthusiasm and insight, and M. Kardar for his guidance and comments. S.C. thanks G. McKinley for his support. Supported by NSF grant DMR-98-05833 (R.d.S.), NASA grant NAG3-2155 (S.C.), and the Karl van Tassel Chair at MIT (L.M.).

24 June 1999; accepted 5 January 2000

## Control of Thickness and Orientation of Solution-Grown Silicon Nanowires

Justin D. Holmes,<sup>†</sup> Keith P. Johnston, R. Christopher Doty, Brian A. Korgel\*

Bulk quantities of defect-free silicon (Si) nanowires with nearly uniform diameters ranging from 40 to 50 angstroms were grown to a length of several micrometers with a supercritical fluid solution-phase approach. Alkanethiol-coated gold nanocrystals (25 angstroms in diameter) were used as uniform seeds to direct one-dimensional Si crystallization in a solvent heated and pressurized above its critical point. The orientation of the Si nanowires produced with this method could be controlled with reaction pressure. Visible photoluminescence due to quantum confinement effects was observed, as were discrete optical transitions in the ultraviolet-visible absorbance spectra.

One-dimensional quantum wires are expected to play a vital role as both interconnects and functional components in future mesoscopic electronic and optical devices and also to provide an opportunity to test fundamental quantum mechanical concepts (1, 2). As the wire diameter approaches the carrier de Broglie wavelength, quantum confinement effects shift band gap energies and, in Si, induce visible photoluminescence (3). The electronic and optical prop-

erties of the nanowires strongly depend on size; therefore, size control and tunability are key to the success of any method of synthesizing quantum wires. Dimensionality also affects the material properties of nanowires. The absence of translational symmetry in Si could profoundly affect the electronic properties: Bulk Si is an indirect semiconductor with a band gap of 1.1 eV, whereas linear polysilane chains exhibit a 3.89-eV direct gap (4). The lattice orientation in a wire can provide a tuning parameter, unavailable in quantum dots, to adjust material properties to suit particular applications. In carbon nanotubes, for example, the bonding geometry and orientation profoundly affect the electronic structure and can lead to either metallic or insulating behavior (5). Calculations for Si nanowires

Department of Chemical Engineering and Texas Materials Institute, University of Texas, Austin, TX 78712, USA.

\*To whom correspondence should be addressed. E-mail: korgel@mail.che.utexas.edu

<sup>†</sup>Present address: Department of Chemistry, University College Cork, Ireland.